

Supplementary Figure 1. Western Blot analysis of total Nephrin protein levels in glomeruli isolated from kidneys of newborn CRE[+];NOTCH-IC mice and control littermates. (A) Shown are Western Blot images for Nephrin (upper panel), WT1 (middle panel), and ACTIN (lower panel) in glomerular lysates from three CRE[-];NOTCH-IC (lanes 1-3) and four CRE[+];NOTCH-IC (lanes 4-8) newborn mice. Lysates were prepared from glomeruli isolated from newborn mouse kidneys by iron oxide perfusion followed by magnetic separation. Lysates were separated by SDS-PAGE, transferred onto PVDF membrane, and probed with anti-Nephrin to detect total Nephrin. Membranes were stripped and re-probed with anti-WT1 to detect WT1 protein, which was used as a surrogate measure of podocyte number to control for sample bias. Membranes were stripped a third time and re-probed with anti-Actin to detect Actin as a loading control. The leftmost lane depicts molecular weight standards. (B) Graphic representation of Nephrin (upper panel) and WT1 (lower panel) protein levels as determined semi-quantitatively by band densitometry. Band density was measured using image analysis software. Values for each lane were normalized to band density for corresponding actin loading control and expressed in arbitrary units (pixel number). White bars depict the mean value of measurements from three CRE[-];NOTCH-IC mice. Black bars show the mean measurement from four CRE[+];NOTCH-IC mice. Error bars denote S.E. (upper panel) No significant difference in total Nephrin protein levels was detected in glomerular lysates from CRE[+];NOTCH-IC mice compared to CRE[-];NOTCH-IC controls. (lower panel) Likewise, WT1 levels were comparable in lysates of CRE[+];NOTCH-IC and control glomeruli, which inferred that total Nephrin levels were not biased by differences in podocyte number between lysate samples.

Supplementary Figure 2. Immunostaining patterns for ZO-1, Neph1 and Podocin in glomeruli of newborn CRE[+];NOTCH-IC mice and control littermates. Shown are merged multi-channel images of representative mouse glomeruli within kidney tissue sections. Sections were imaged following indirect immunofluorescence multi-labelling with anti-MYC to detect ^{MYC}NOTCH-IC (blue) and either anti-ZO-1 (A, B; green), anti-Neph1 (C, D; brown staining), or anti-Podocin (E, F; red) to detect corresponding proteins. (A, C, E) CRE[-];NOTCH-IC (control). (B, D, F) CRE[+];NOTCH-IC. Arrowheads illustrate staining for ZO-1 (B), Neph1 (D), or Podocin (F) in cells where ^{MYC}NOTCH-IC is also detected by anti-MYC. (E' and F') Sections stained with anti-Podocin were also stained with anti-Nephrin. Shown are merged images depicting anti-Podocin (red) and anti-Nephrin (green) staining patterns in the same glomeruli shown in (E) and (F). Red arrowheads in (F') illustrate regions of attenuated staining for both Podocin and Nephrin.

Supplementary Figure 3. Scoring of anti-Nephrin staining in podocytes of CRE[+];NOTCH-IC transgenic mice. Mouse kidney tissue sections were co-incubated with anti-Nephrin, anti-WT1, and anti-MYC antibodies to reveal indirect immunofluorescence staining patterns for Nephrin protein (green), podocyte nuclei (red), and ^{MYC}NOTCH-IC protein (blue), respectively, within glomeruli. (Far left panels) Dual channel images showing Nephrin and WT1 staining. (Left-center panels) Dual channel images of the same glomeruli showing staining for ^{MYC}NOTCH-IC and WT1. (Right-center panels) Merged images of anti-Nephrin, anti-WT1, and anti-MYC staining for the same glomeruli. (Far left panels). Magnified views of areas denoted by corresponding white boxes in mid-right panels. White arrows denote the location of WT1-positive cells which were also positive for ^{MYC}NOTCH-IC. Glomeruli were randomly selected for semi-quantitative analysis of Nephrin immunostaining. Within each

glomerulus analyzed, podocytes were assigned a score (1, 2, or 3) based on the pattern of anti-Nephrin antibody staining along the longest basolateral edge of each podocyte. Score 1 corresponded to a homogeneous, continuous, linear pattern of anti-Nephrin staining (top row). Score 2 was assigned to podocytes which exhibited a non-homogeneous, non-continuous, granular anti-Nephrin staining pattern (middle row). Score 3 corresponded to absent anti-Nephrin staining (bottom row). For each glomerulus, the number of podocytes having scores of 1, 2, and 3 (white arrowhead) was determined and expressed as a percent of the total number of podocytes per glomerulus. The mean total number of WT1-positive podocytes per glomerulus was similar for 21 glomeruli from 3 CRE[-];NOTCH-IC mice (13±1) as well as from 56 glomeruli from 3 CRE[+];NOTCH-IC mice (13±1), and 23 glomeruli from 3 CRE[+];NOTCH-IC;RBP^{KO} mice (16±1). Also, the mean number of [WT1,MYC]-double positive cells and the corresponding percent of total WT1-positive podocytes were similar for CRE[+];NOTCH-IC (4.7±0.4; 36±3%, respectively) and CRE[+];NOTCH-IC;RBP^{KO} mice (4.0±0.5; 24±3%, respectively).

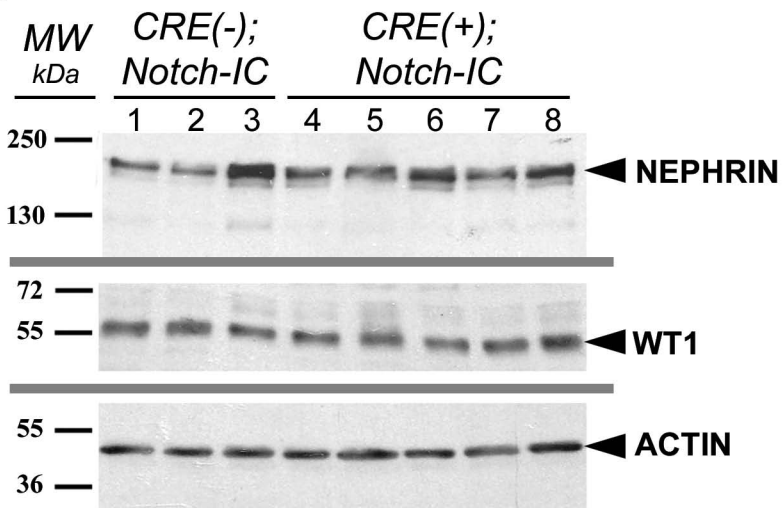
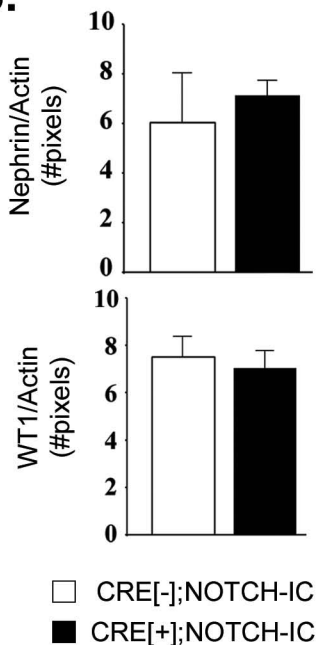
Supplementary Figure 4. mRNA expressions for a subset of slit-diaphragm-associated genes in glomerular extracts of CRE[+];NOTCH-IC mice and control littermates. Graphic representation of real time RT-PCR results for *Nphs1*, *Nphs2*, *Kirrel1* (shown as Neph1), *Kirrel3* (shown as Neph2), *Kirrel2* (shown as Neph3), *Fat1*, *Tjp1* (shown as ZO1), *Cd2ap*, and *Wt1* expressions in glomerular extracts from one week old mice as determined by the Δ Ct method of relative quantification normalized to *Gapdh*. Values represent the mean of duplicate measurements on extracts from four mice per genotype. Error bars denote S.E. P-values correspond to comparison between CRE[+];NOTCH-IC (black bars) and CRE[-];NOTCH-IC (grey bars) mice using the Mann Whitney U test.

Supplementary Figure 5. Dynasore is an effective inhibitor of dynamin-dependent endocytosis in HEK293T cells as revealed by analysis of transferrin uptake. Shown are representative images of HEK293 cells cultured in the absence (A, B, C) or presence (D, E, F) of Dynasore 160 μ M. Cells were incubated with AlexaFluor488-conjugated transferrin (30 μ g/mL) at 37°C for 1 hour, washed, fixed, and permeabilized prior to imaging. (A and D) Green channel images depicting cellular distribution of transferrin. (B and E) Red channel images of same cells shown in (A) and (D) revealing WGA staining. (C and F) Merged images. Nuclei were counterstained with DAPI (re-colored as grey). Insets show magnified views of area represented by small white box in the corresponding image. (A-C) Transferrin was abundantly detected within the cytoplasmic compartment of cells treated with vehicle (DMSO) alone. (D-F) Effective inhibition of transferrin uptake by Dynasore was revealed by a significant reduction in the amount of AlexaFluor-transferrin detected within the cytoplasm of Dynasore-treated cells. (G) Graphic representation of transferrin uptake as determined by measuring cytoplasmic AlexaFluor-transferrin immunofluorescence intensity. The bar chart shows internalized transferrin expressed as the number of pixels $\times 10^3$ per μm^2 . +DMSO, vehicle alone. +DYNO., Dynasore 160 μ m. DYNO vs. DMSO: 15 ± 1 vs. 21 ± 2 , $P=0.006$.

Supplementary Figure 6. Bar chart showing results of total cell cholesterol measurement in untransfected HEK293T cells pre-treated with increasing doses of M β CD as determined by spectrophotometric assay (see Methods). Values represent the mean of triplicate measurements at each dose and are expressed as a per cent of the difference from baseline (i.e. M β CD 0 mM). Error bars denote S.E.

Supplementary Figure 7. Electron photomicrographs depicting ultrastructural appearance of podocyte cell bodies, foot processes, and slit diaphragms in glomeruli of newborn CRE[+];NOTCH-IC mice. Shown are representative photomicrographs obtained by scanning electron microscopy (A through D) and transmission electron microscopy (E through H). (A, C, E, G) Images from CRE[-];NOTCH-IC (control) mice. (B, D, F, H) Images from CRE[+];NOTCH-IC mice. (A, B) Low power images of glomeruli revealing apical view of podocyte cell bodies; original magnification 5,000X. (C, D) High power images of regions represented by black boxes in (A) and (B), which illustrate podocyte foot processes (white arrows); original magnification 15,000X. Podocyte foot processes appear as elongated, slender, interdigitating structures in CRE[-];NOTCH-IC mice (C). In contrast, foot processes in CRE[+];NOTCH-IC mice (D) appear shorter and more randomly distributed. (E, F) Low power transmission electron micrographs showing representative glomerular capillary loops in cross-section. Podocyte foot processes (black arrows) line the glomerular basement membrane and underlying glomerular capillary loops; original magnification, 5000X. Black arrowhead in (F) reveals a focal area of foot process fusion (effacement) in a glomerular capillary loop from CRE[+];NOTCH-IC mouse. (G, H) High power images showing appearance of filtration slits between podocyte foot processes. White arrowheads and white arrow in (G) show electron-dense slit diaphragms in two views. White arrows in (H) illustrate narrowed filtration slit. Black arrowhead in (H) shows fused podocyte foot process. The mean length of GBM analyzed per imaged field was not significantly different between CRE[+];NOTCH-IC and control mice (mean GBM length, CRE[+];NOTCH-IC vs. CRE[-];NOTCH-IC: $2.62 \pm 0.03 \mu\text{m}$ vs. $2.74 \pm 0.04 \mu\text{m}$; $P=0.07$).

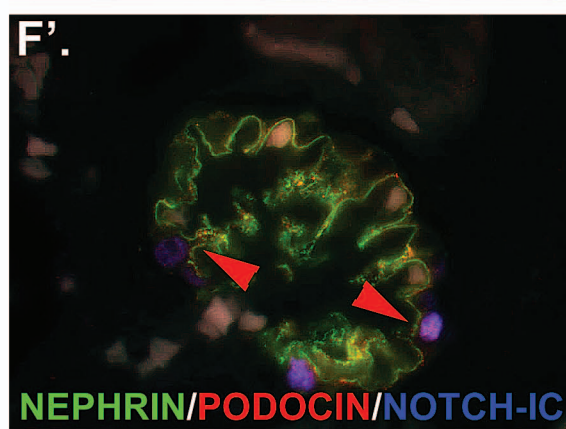
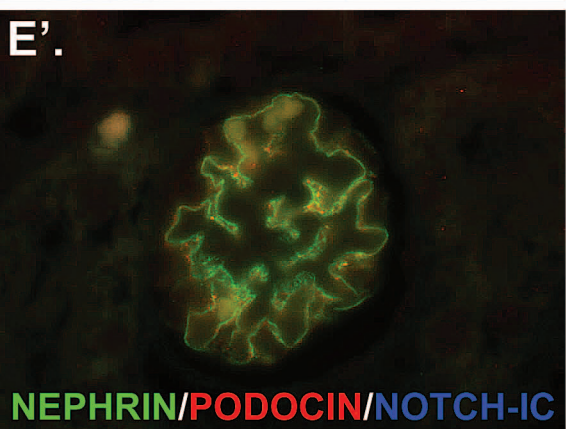
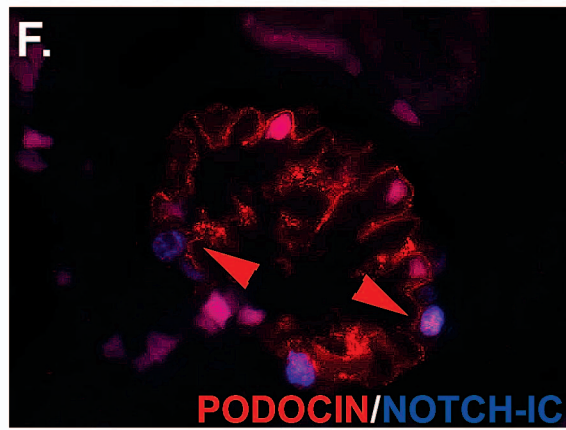
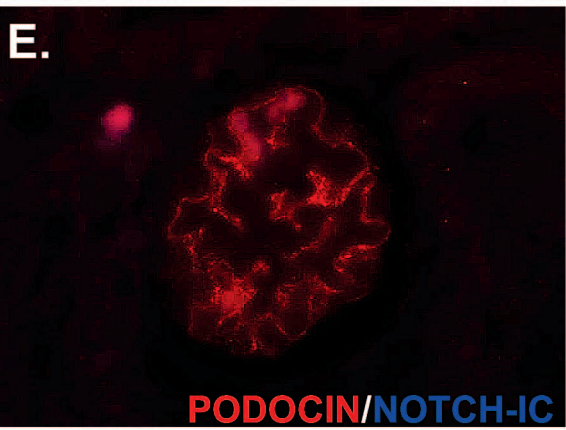
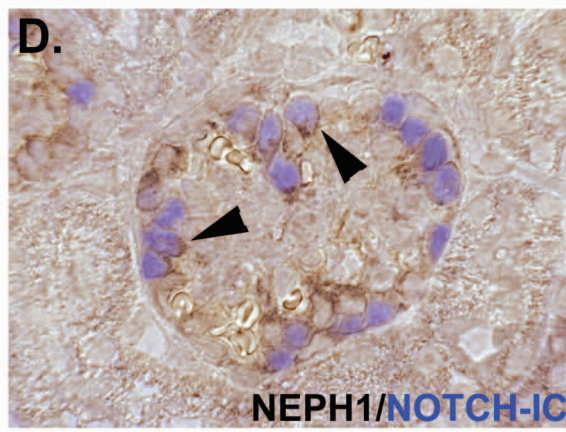
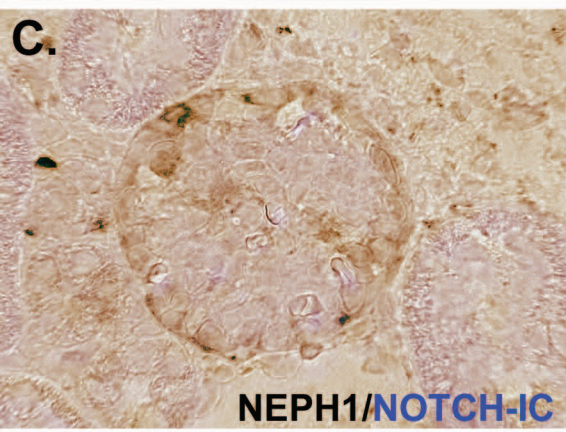
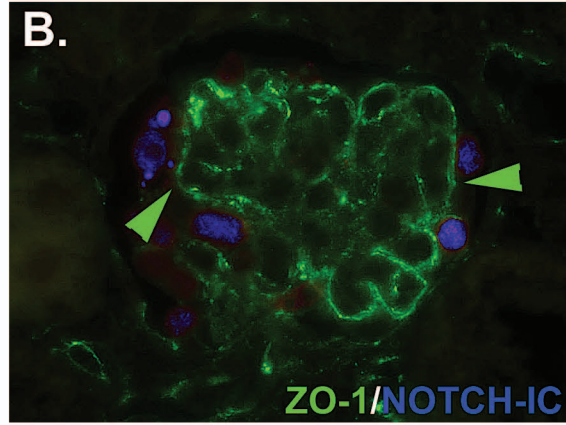
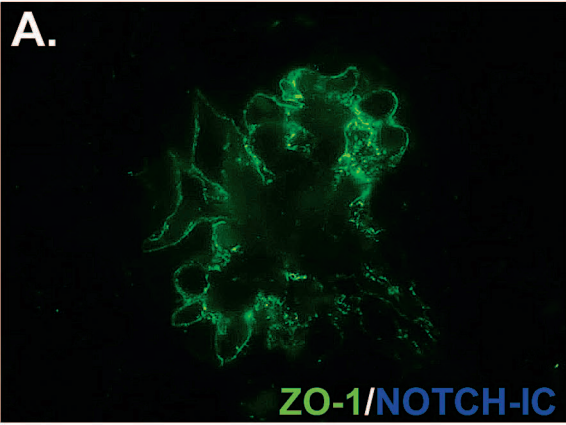
Supplementary Figure 8. Anti-Grp78 immunostaining patterns in glomeruli of CRE[+];NOTCH-IC and control mice. Shown are images of representative glomeruli in kidney tissue sections of two week old (A) CRE[-];NOTCH-IC and (B) CRE[+];NOTCH-IC mice. Black arrows denote podocytes staining positively for Grp78.

A.**B.**

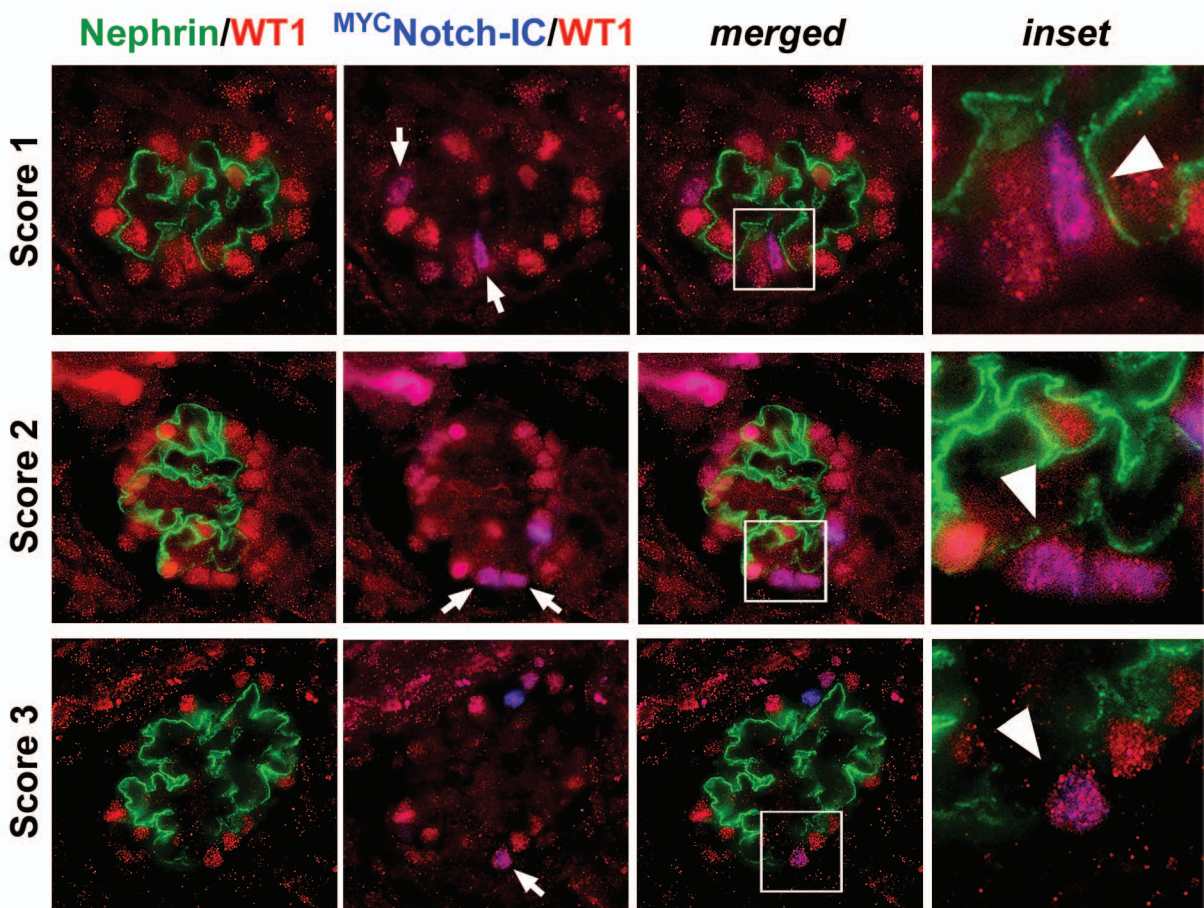
Supplementary Figure 1

CRE[-];NOTCH-IC

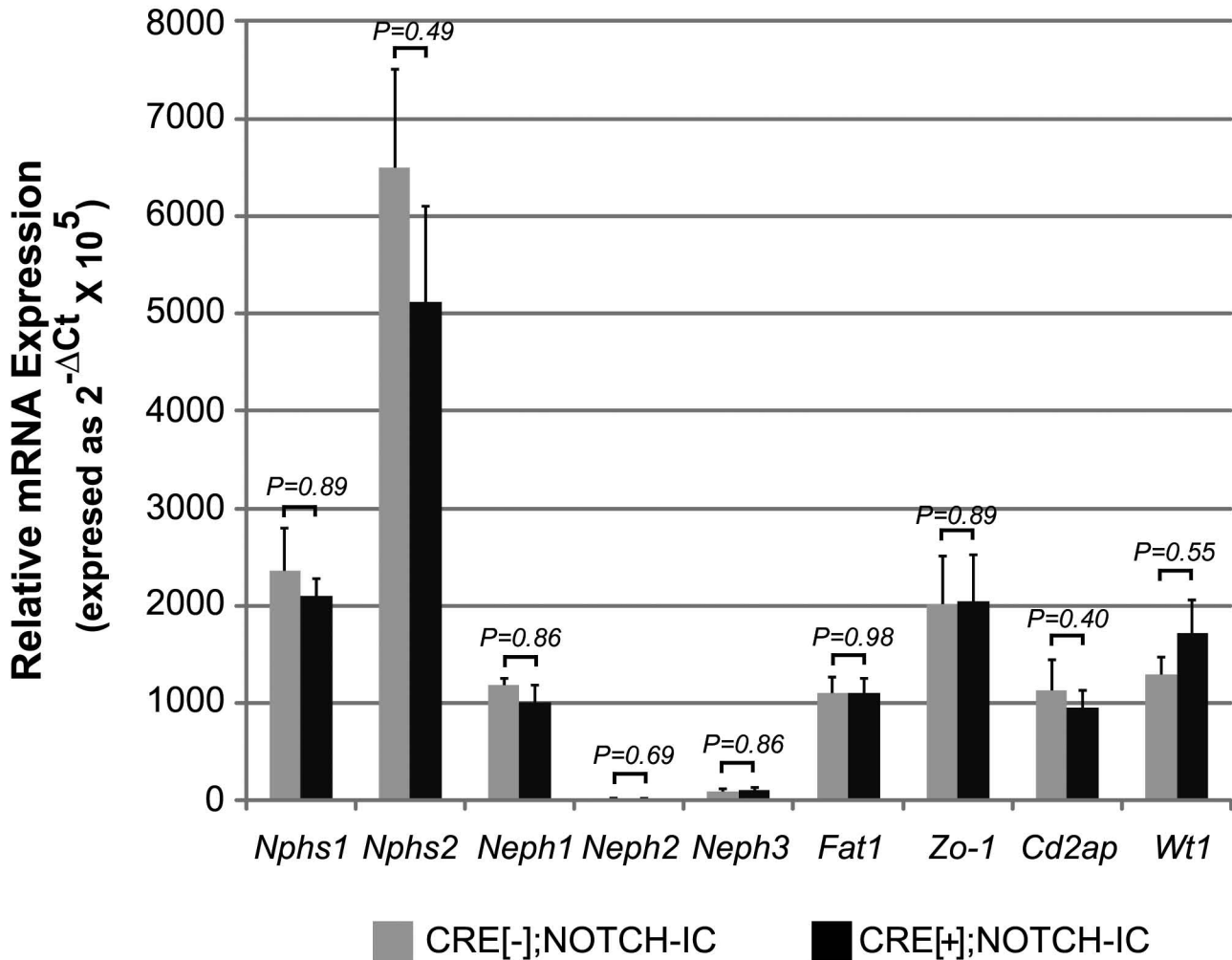
CRE[+];NOTCH-IC



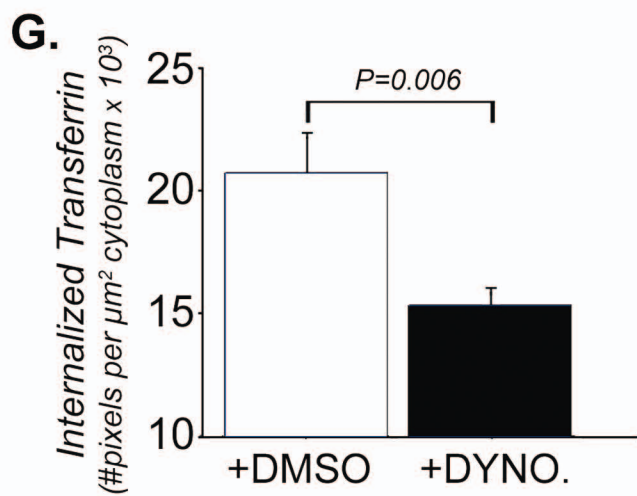
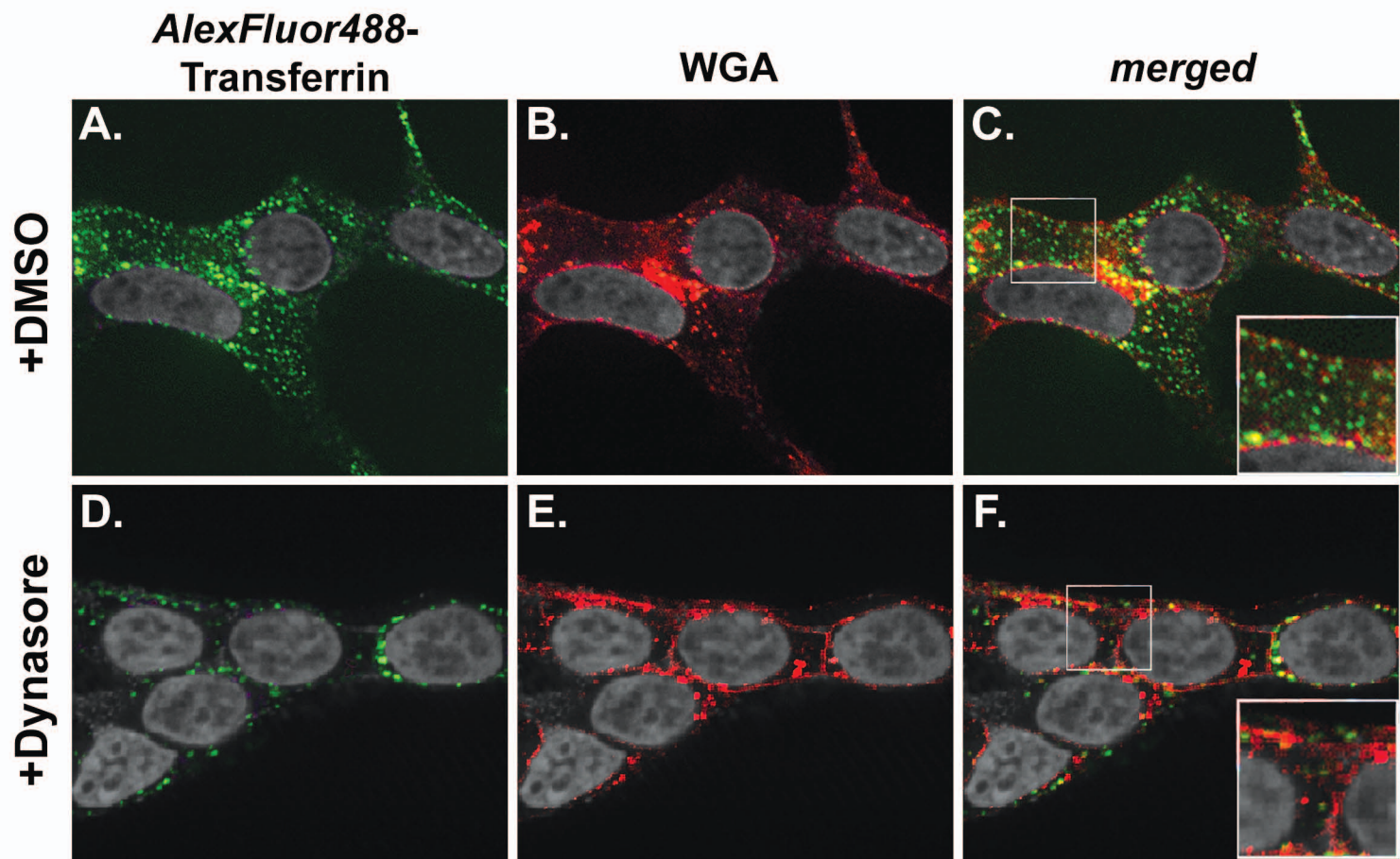
Supplementary Figure 2



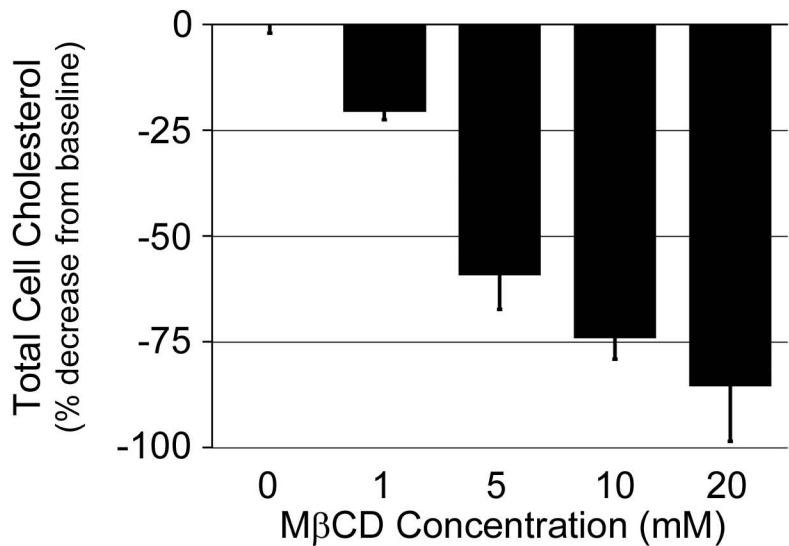
Supplementary Figure 3



Supplementary Figure 4



Supplementary Figure 5

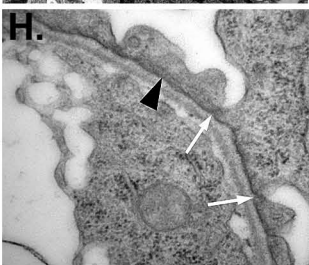
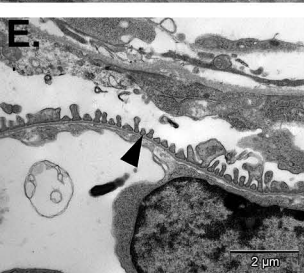
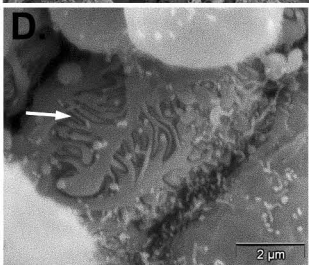
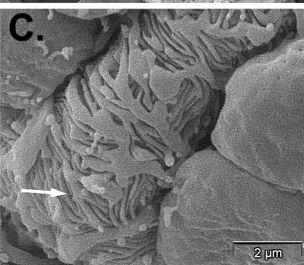
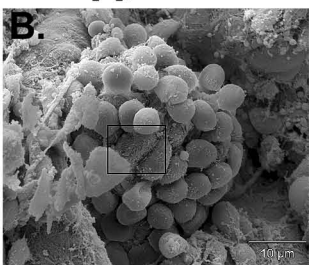


Supplementary Figure 6

CRE[-];NOTCH-IC

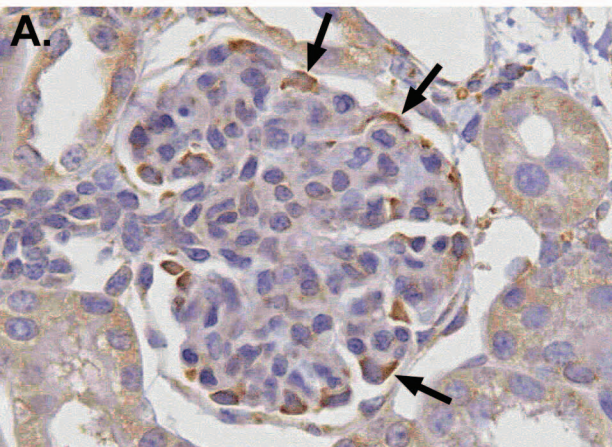


CRE[+];NOTCH-IC

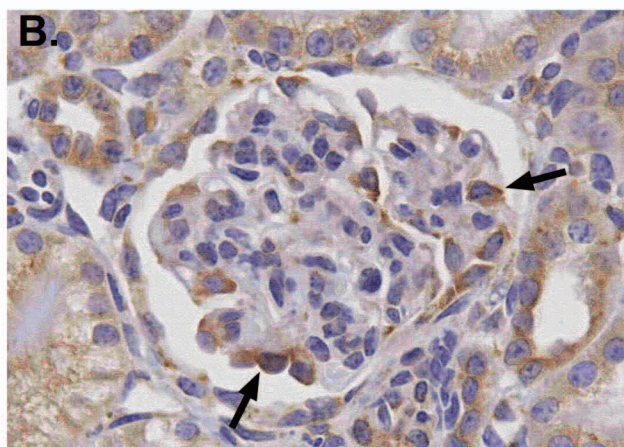


Supplementary Figure 7

CRE[-];NOTCH-IC



CRE[+];NOTCH-IC



Supplementary Figure 8